Automatic Reorientation of Three-Dimensional, Transaxial Myocardial Perfusion SPECT Images

Guido Germano, Paul B. Kavanagh, Hsiao-Te Su, Marco Mazzanti, Hosen Kiat, Rory Hachamovitch, Kenneth F. Van Train, Joseph S. Areeda and Daniel S. Berman

Department of Medical Physics and Imaging, Division of Nuclear Medicine, Department of Imaging and the Division of Cardiology, Department of Medicine, Cedars-Sinai Research Institute, Cedars-Sinai Medical Center; and Division of Nuclear Medicine and Biophysics, Department of Radiological Sciences, and the Department of Medicine, UCLA School of Medicine, Los Angeles, California

We developed a completely automatic technique to reorient transaxial images into short-axis (oblique) myocardial perfusion SPECT images. **Methods:** The algorithm starts by isolating (segmenting) the left ventricle (LV) myocardium using a combination of iterative clusterification and rule-based location/size/shape criteria. The three-dimensional, mid-myocardial LV surface is initially estimated as the locus of the trilinearly interpolated maxima for the count profiles originating from the center of mass of the segmented LV. The final mid-myocardial surface is obtained by iteratively applying this process, incorporating additional constraints of shape and texture and using the nonsegmented, nonthresholded transaxial image to obtain information on hypoperfused areas of the myocardium. It is then fitted to an ellipsoid, of which the major axis is assumed to represent the long axis of the LV, and the three-dimensional image volume is resliced perpendicularly to it. **Results:** The algorithm was retrospectively applied to 400 dual-isotope studies (200 rest ^{201}Tl, 200 stress ^{99m}Tc-sestamibi) from 200 consecutive patients. Segmentation was successful in 394/400 (98.5%) of the patients. The reproducibility of computer-based reorientation was perfect and significantly better than either intraobserver or interobserver reproducibility. **Conclusion:** Automatic reorientation offers the potential for consistently faster and more accurate image processing and analysis and is an important step towards totally operator-less management of myocardial perfusion SPECT data.

Key Words: transaxial myocardial perfusion; single-photon emission computed tomography; automatic reorientation expert systems

J Nucl Med 1995; 36:1107–1114

The reorientation of tomographic transaxial images of the myocardium into short-axis images is a common practice in both SPECT and PET. Transaxial images are the direct result of tomographic reconstruction perpendicular to the long axis of the patient, and, therefore, are usually not perpendicular to the long axis of the left ventricle (LV). Their cutting through the myocardium at an oblique angle leads to regional differences in the apparent myocardial thickness, which, in turn, causes artifactual inhomogeneities in the regional recovery coefficients and relative count densities due to the partial volume effect phenomenon (*1*). Another limitation of transaxial images is that the heart's orientation in the human chest is patient-specific. Visual interpretation of transaxial images suffers from this nonstandardized orientation, resulting in lower reported sensitivity and specificity for the detection of perfusion defects (*2,3*). Short-axis images, which are perpendicular to the LV's long axis, allow standardization of myocardial perfusion SPECT display and interpretation; in addition, they make it possible to present three-dimensional information in two-dimensional polar maps, the standard for quantification and display of scintigraphic myocardial perfusion data (*4*).

Reorientation of myocardial perfusion SPECT tomograms typically requires manual selection of a reference transaxial image and manual drawing of the LV's long-axis component in the transaxial plane (Fig. 1, left). This operation is then repeated for another tomographic plane (the sagittal or vertical long-axis plane) perpendicular to the transaxial reference plane and parallel to the long-axis component in that plane (Fig. 1, center). The LV's long-axis orientation in the transaxial and vertical long-axis planes defines its orientation in the three-dimensional space, which in turn defines the change-of-coordinate matrix necessary to reslice the image volume perpendicularly to the LV's long axis (Fig. 1, right) (*5*). This manual procedure is not only time consuming, but it is also subjective. It has been shown that if reorientation is not performed correctly, artifacts may result (*6,7*), as demonstrated in Figure 2. Together with the selection of apical and basal slices for polar map generation, manual selection of the LV's long-axis for reorientation is probably the most variable step in processing myocardial perfusion SPECT. To promote standardization and obviate inter- and intraob-

Received Aug. 12, 1994; revision accepted Nov. 11, 1994.

For correspondence or reprints contact: Guido Germano, PhD, Nuclear Medicine Physics, Cedars-Sinai Medical Center A047 N., 8700 Beverly Blvd., Los Angeles, CA 90048.

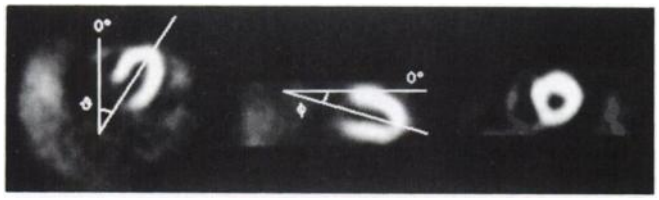

FIGURE 1. Manual reorientation of transaxial myocardial SPECT images. A midventricular transaxial image is selected, the LV long axis manually drawn and the transaxial angle ϑ determined (left). The same procedure is performed on a vertical long-axis or sagittal image, resulting in the determination of the vertical long-axis angle ϕ (center). Reformatting the image volume perpendicularly to the LV long axis produces a set of short-axis images (right).

server variability, various algorithms have aimed at automating reorientation.

In previous efforts to automatically derive the orientation of the LV's long axis, Cooke et al. (*8*) identified the myocardial apex as the point of maximum gradient along the maximal-count circumferential profile in an operator-selected, midventricular transaxial image and used the line of minimum counts passing through the apex as a proxy for the LV's long axis. In similar fashion, He et al. (*9*) selected a mid-ventricular transaxial and a mid-ventricular sagittal image, manually marked the myocardial apex and base in those images, then examined a series of parallel-count profiles from apex to base in both images. The locus of the local minima along those profiles represented the projection of the LV's long axis in the two image planes, from which its three-dimensional location could be determined. Another approach by Cauvin et al. (*10*) requires that the location of the LV be identified and the LV isolated by manual drawing of a spherical region of interest (ROI) around it. The myocardium is then thresholded at 50% of its maximal activity, binarized and its "skeleton" extracted as the locus of the centers of the maximal spheres included in the binarized volume (*11*). The three-dimensional skeleton of the myocardium is finally fitted to a quadratic surface, whose axis represents the LV's long axis. All these algorithms were developed for and applied to ^{201}Tl SPECT data exclusively, and required some degree of operator interaction, falling short of completely automating the reorientation process.

In the current study, a new method has been developed to segment the LV in the transaxial image volume. Extraction of the maximal-count myocardial surface is performed on the segmented LV with methodology similar to circumferential profiles generation in short-axis images. The extracted surface is refined by incorporating additional constraints of shape and texture and using the nonsegmented, nonthresholded transaxial image to obtain information on hypoperfused areas of the myocardium. Finally, the surface is fitted to a quadratic surface and its long axis determined as in Cauvin's approach (*10*). The algorithm was retrospectively tested on a large number of patients who underwent both a ^{99m}Tc-sestamibi and ^{201}Tl SPECT studies, to determine its percentage of success in completely automating the reorientation process, as well as its reproducibility and agreement with manual reorientation.

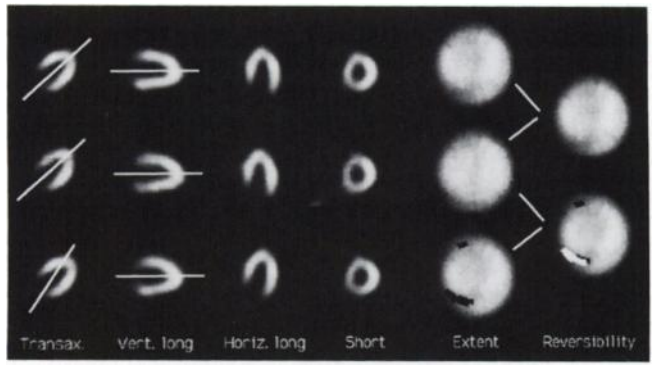

FIGURE 2. Effect of incorrect reorientation on quantitative polar map output. Top row shows (left to right) representative midventricular transaxial, vertical long-axis, horizontal long-axis and short-axis images, together with the defect extent polar map for a properly reoriented, stress ^{99m}Tc-sestamibi SPECT study of a normal patient. The center row shows corresponding images for a rest ^{201}Tl SPECT study of the same patient, also properly reoriented. The bottom row shows the same study as in the top row, only incorrectly reoriented (note the excessive slope of the long axis drawn on the transaxial image, resulting in a tilted horizontal long-axis image). On the far right, the two polar maps are the stress-rest reversibility polar maps for the correctly (top) and incorrectly (bottom) reoriented stress-rest image pairs.

METHODS

Our reorientation algorithm was retrospectively tested on 200 consecutive clinical patients undergoing a rest ^{201}Tl/stress ^{99m}Tc-sestamibi "separate acquisition dual-isotope" SPECT protocol (*12*). In this protocol, a rest ^{201}Tl study is followed by injection of ^{99m}Tc-sestamibi at peak exercise and acquisition of a second study. Consequently, ^{201}Tl images are uncontaminated by ^{99m}Tc, and ^{99m}Tc-sestamibi images are only minimally affected by ^{201}Tl crosstalk (*13*). Half of the studies (100 rest, 100 stress) were acquired on a dual-detector camera and the other half on a single-detector camera. Both cameras used LEHR collimation, modified step-and-shoot detector rotation (*14*), 64 projections over 180° and the same processing computer (Pegasys, ADAC Laboratories, Milpitas, CA). The projection data were reconstructed over 180° (45° RAO to LPO) using filtered backprojection and no attenuation correction. The backprojection filter was a ramp multiplied by a Butterworth filter of order = 2.5 and critical frequency = 0.33 Nyquist for ^{99m}Tc-sestamibi, order = 5 and critical frequency = 0.25 Nyquist for ^{201}Tl (Nyquist frequency = 0.78 cycles/cm for the Vertex, 0.82 cycles/cm for the Orbiter). The resulting transaxial images for all 400 studies were collected on optical disk and transferred to a standalone workstation (Sun SPARC IPX, Mountain View, CA) running the automatic reorientation software, which processed them in batch mode. Reorientation of the transaxial data sets had been independently performed by two experienced operators: one (A) at the time of the individual studies' collection, and the other (B1, blinded to previous manual and automatic results) after all studies had been acquired. The second operator reoriented the data again 1 mo later (B2), for intraobserver variability assessment. Unlike operator A, operator B1/B2 had participated in the development of the automatic reorientation method and was therefore aware of the criteria on which the

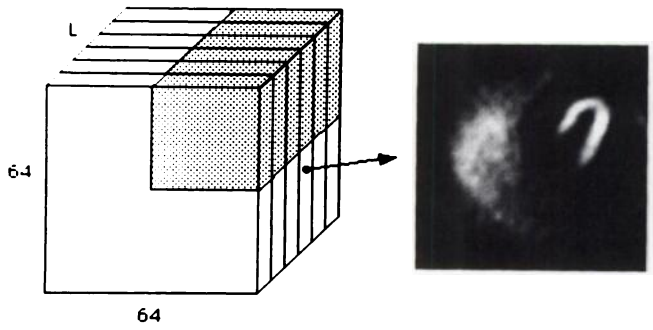

FIGURE 3. Automatic segmentation of the LV myocardium. The initial threshold used in the clusterification process is based on the maximal count activity in the upper right quadrant of the transaxial image volume, i.e., the area that the heart should occupy if the study has been correctly acquired and reconstructed. When present, hepatic activity is generally confined to the left half of the transaxial image volume, while splenic or intestinal activity is likely to appear in the lower right quadrant.

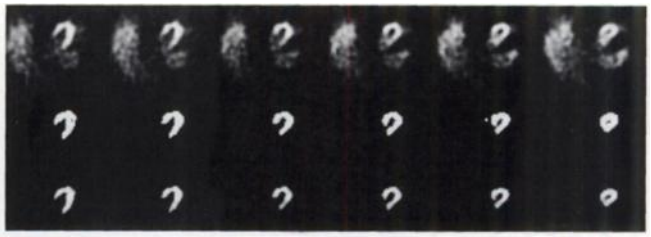

FIGURE 4. Automatic segmentation of the LV myocardium. Thresholding, clusterification and rule-based cluster selection and refinement by eroding/dilating techniques generate a binary mask (center row) from the original transaxial image volume (top row). Multiplying the mask by the original image isolates the LV myocardium (bottom row).

method is based. The following comparisons were made, for both the ^{201}Tl and the ^{99m}Tc-sestamibi data: (1) automatic algorithm versus operators A, B1 and B2; (2) automatic algorithm versus itself (algorithm reproducibility); (3) operator B1 versus B2 (intraobserver reproducibility); and (4) operator A versus operator B1 (interobserver reproducibility). In all cases, the parameters compared were the angle ϑ between 12 o'clock and the LV's long axis (computed clockwise) in the transaxial plane, and the angle ϕ between 3 o'clock and the LV's long axis (also computed clockwise) in the vertical long-axis plane (Fig. 1). These two angles are determined directly in the manual reorientation technique, which is based in the two-dimensional space, and were derived from the three-dimensional orientation of the LV's long axis in the automatic technique. The reproducibility values determined in the last three comparisons were also compared to assess whether statistically significant differences existed between them.

Left Ventricular Segmentation

The automatic reorientation algorithm starts by segmenting the LV. The maximal voxel count value C_{max} in the upper right quadrant of the 64 × 64 × L (L < 64) transaxial image volume (Fig. 3, left) is calculated; if the study has been correctly acquired and reconstructed, that regional maximum is likely to correspond to the myocardium (Fig. 3, right). The entire transaxial volume is then thresholded to 50% of C_{max}, binarized and the binary clusters in the volume determined. Each cluster, or set of connected voxels, is constructed by depth-first search from a seed voxel (the first nonzero voxel encountered while scanning the transaxial volume from one of its corners). Unlike a breadth-first search, a depth-first search explores a path of voxels as deeply as possible before switching to an alternate path (*15*).

Once a cluster has been identified, its location is marked, its voxels are zeroed and the algorithm continues. When all clusters have been determined, those physiologically too small (<50 ml) to represent the LV myocardium are eliminated. If only one cluster remains and its volume is smaller than 250 ml, the cluster is assumed to correctly identify the LV myocardium. If two or more clusters remain (suggesting that thresholding was successful in separating the LV from other "hot" structures), the one closest to the center of the upper right quadrant of the transaxial image volume is chosen. In either case, if the candidate LV cluster's volume is greater than 250 ml (suggesting that spurious hepatic, splenic or intestinal activity is still "connected" to that in the LV), "erosion" of the cluster is performed by raising the threshold in 5% steps from the original value of $C_{max}/2$, until the cluster is broken into two or more pieces.

The two larger subclusters are selected and assigned to the liver and the LV myocardium (again, based on likely location considerations). Then, dilation of both clusters is performed by iteratively adding 1-voxel wide layers of voxels, checking every voxel in each layer to ensure that its addition will not reconnect the clusters. Dilation is continued until the original $C_{max}/2$ threshold is reached. The binary cluster representing the LV is used as a mask in the subsequent phases of the algorithm. An example of segmentation for a patient study with considerable hepatic and intestinal uptake is shown in Figure 4.

Mid-Myocardial Surface Extraction and Fit

The center of mass (COM) of the three-dimensional binary mask segmenting the LV myocardium is chosen as the origin of the sampling coordinate system. If segmentation of the LV was successful, the COM will be located within the LV cavity, even in the presence of large perfusion defects. Radial count profiles originating from the COM are generated to achieve three-dimensional, spherical sampling of the product of the binary mask and the transaxial image volume (Fig. 4, bottom). The locus of the profiles' first maxima identifies the maximal count myocardial surface, which is an acceptable proxy for the mid-myocardial surface. Sampling is every 10° longitudinally (18 total) and every 10° latitudinally (36 total), resulting in 684 count profiles. It should be noted that a variable, potentially large number of these profiles is uniformly zero. In fact, both the basal portion of the myocardium at the valve plane and all perfusion defects will correspond to "holes" in the mask, for which no maxima are returned. A fit of the mid-myocardial surface to a quadratic surface is performed as reported by Cauvin et al. (*10*), and the long axis of the quadratic surface is considered an initial estimate of the long axis of the LV. The surface extraction process is then repeated using a new origin for the sampling coordinate system, determined as the projection of the original COM onto the estimate of the long axis. This approach seeks to obviate errors in mid-myocardial surface extraction, especially in cases where the original COM is close to the wall due to extensive perfusion defects. The process is iterated until the long-axis angular variation is less than 0.5°, which generally requires two to three iterations.

We now have an estimate of the mid-myocardial surface containing "perfusion holes," plus the quadratic surface (ellipsoid) that best fits it. To incorporate perfusion data from underperfused areas into the fit (fill the holes), a set of myocardial "likelihood

profiles" (24 latitudinally, 32 longitudinally) is generated by extracting count profiles normal to the ellipsoid from the unmasked and nonthresholded image and convolving them with a feature detector consisting of the double derivative of a Gaussian with a s.d. σ = 10 mm. The s.d. value of 10 mm was chosen based on expected feature size and camera resolution and observed LV myocardial count profiles, which are seen to approximate Gaussians with standard deviations of approximately 10 mm. The number of samples was chosen so that a sampling frequency of approximately 5 mm from count profile to count profile at the myocardium would result for a typical LV geometry (75 mm from apex to base, 50 mm from superior to inferior wall).

The local maxima of these profiles are extracted (there is generally at least one local maximum per profile). The final mid-myocardial surface is then defined as that set of surface points, one per profile, which minimizes the sum of the cost of each surface point. The cost of each surface point is defined as a weighted sum of the deviation between its surface normal and its corresponding ellipsoidal normal and a nonlinear function of its distance from, and the magnitude of, each of the local maxima of the likelihood profile. In particular, the cost C(x, y) of each surface point (x, y) is defined as:

$$C(x, y) = k_x(D(x + 1, y) - D(x, y)) + k_x(D(x - 1, y) - D(x, y)) + k_y(D(x, y + 1) - D(x, y)) + k_y(D(x, y - 1) - D(x, y)) + \sum_{i=1}^{N} r(D(x, y) - d_i, w_i), \quad \text{Eq. 1}$$

and

$$r(d, w) = \begin{cases} K_m w^g \frac{|d|}{d_0}, & |d| < d_0 \\ K_m w^g \frac{d_0}{|d|}, & |d| \geq d_0, \end{cases} \quad \text{Eq. 2}$$

where

(x, y) is the surface point with longitude x and latitude y;
D(x, y) is the distance of the surface point (x, y) from the basis ellipsoid;
k_x = 0.55 is the cost weight given to the variation in distance between adjacent longitudines;
k_y = 0.275 is the cost weight given to the variation in distance between adjacent latitudes;
N is the number of candidate points (local maxima) for the count profile through the surface point (x, y);
d_i is the distance of the candidate point i from the basis ellipsoid;
w_i is the weight of the candidate point i;
r(d, w) is the cost associated with being distance d from a candidate point with weight w;
k_m = 1.5 is the cost weight given to the variation in distance between a surface point and a corresponding candidate point;
g = 0.5 is the amount by which all candidate point weights w_i are exponentiated; and
d_0 = 3 mm is the threshold distance beyond which the cost for variation in distance between a surface point and a candidate point starts to decrease.

An ellipsoid is finally fitted to this myocardial surface and the resulting long axis returned as that of the LV. The entire segmentation, surface extraction, fitting and generation of the reoriented short-axis image volume requires less than 5 sec per study on a Sun SPARC IPX computer (Mountain View, CA) using a X-Windows-based graphical user interface. The entire application software was developed in-house and is easily portable to other Unix platforms utilizing X-windows. We have recently installed it on the beta version of the Pegasys MD display workstation (ADAC Laboratories), based on a Sun SPARC 5 computer, with over a two-fold increase in performance compared to the Sun SPARC IPX.

Statistical Analysis

The first hypothesis tested in this study was whether the values for the transaxial angle ϑ and the vertical long-axis angle ϕ, determined by the automatic reorientation program (Auto), significantly differed from those manually obtained by human observers (A, B1, B2). This hypothesis was tested using a paired t-test that directly compared homologous automatic and manual angular value sets. The angular value sets were also compared using linear regression analysis to obtain a quantitative measure of how closely related the angular values determined by the automatic and the manual methods were. Values of $p < 0.05$ were considered statistically significant.

The second purpose of this study was to assess the reproducibility of the automatic and the manual reorientation methods. The measure of reproducibility used was the magnitude of the r value and the standard error of the estimate (s.e.e.) derived from linear regression analysis, which related two separate angular determinations obtained by repeated application of the same method. We further compared: (1) the reproducibility of the automatic method versus the intraobserver reproducibility; (2) the reproducibility of the automatic method versus the interobserver reproducibility; (3) interobserver reproducibility versus intraobserver reproducibility; (4) intraobserver reproducibility using ^{99m}Tc-sestamibi versus ^{201}Tl images; and (5) interobserver reproducibility using ^{99m}Tc-sestamibi versus ^{201}Tl images. The absolute difference between the two angular determinations associated with each reproducibility test was determined (|Δ angle| in Table 3). For each of the comparisons between reproducibilities, we compared those paired absolute differences using a paired t-test. This was done for both the ϑ and the ϕ angle. All statistical calculations were performed using the Excel® (Microsoft, Redmond, WA) software.

RESULTS

Segmentation of the LV was successful in 394/400 (98.5%) of the studies, with no significative difference between rest ^{201}Tl (five failures) and stress ^{99m}Tc-sestamibi (one failure). Failure is defined as: (1) the absence of LV in the segmented image (four ^{201}Tl); (2) the presence of substantial hepatic or intestinal components in the segmented image (one ^{201}Tl, one ^{99m}Tc); and/or (3) automated determinations of reorientation angles differing by more than 45° from the manually obtained ones (one ^{201}Tl, also in (1)). The user interface allows for the manual placement of a three-dimensional ellipsoidal ROI around the myocardium, thus constraining the segmentation and reorientation process to the image portion within the ROI. This approach was applied to the six patients in whom segmentation failed, always resulting in successful completion of processing. The small stochastic component introduced by the manual ROI placement made it necessary to explicitly evaluate the reproducibility of the automatic reorientation method.

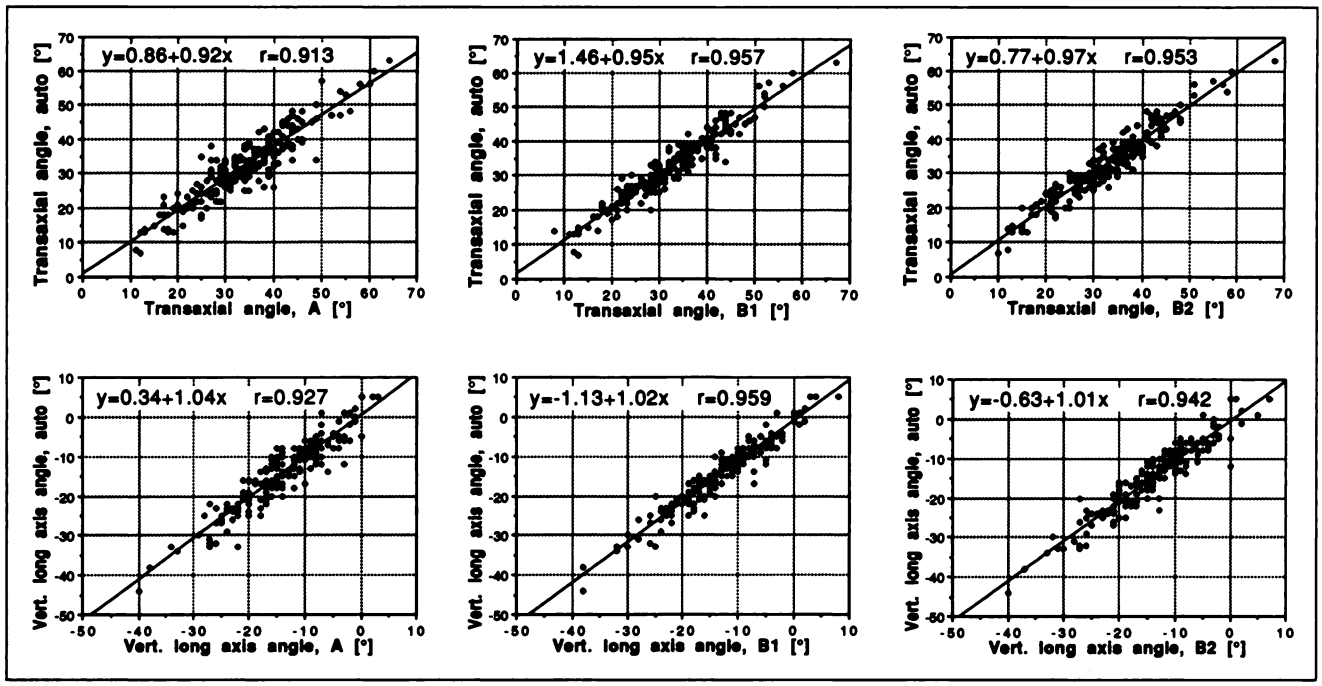

FIGURE 5. Transaxial angles ϑ (top row) and vertical long-axis angles ϕ (bottom row) calculated by the automated software (y axis), compared to the homologous angles manually determined by operators A (left), B1 (center) and B2 (right) for the 200 ^{99m}Tc-sestamibi studies analyzed.

Figure 5 shows the transaxial angles ϑ (top row) and the vertical long-axis angles ϕ (bottom row) calculated by the automated software (y axis) for all ^{99m}Tc-sestamibi studies, compared to the homologous angles manually determined by operators A, B1 and B2 (x axis). Linear regression analysis showed good to excellent agreement between the manual and the automatic technique, with the r values for automatic versus manual A, automatic versus manual B1 and automatic versus manual B2 equal to 0.902, 0.933 and 0.930 (ϑ, ^{201}Tl), 0.913, 0.957 and 0.953 (ϑ, ^{99m}Tc-sestamibi), 0.851, 0.914 and 0.904 (ϕ, ^{201}Tl) and 0.927, 0.959 and 0.942 (ϕ, ^{99m}Tc-sestamibi), respectively. These results are reported in Table 1, together with the s.e.e. for all regressions. The value of s.e.e. was always between 2° and 4°. Paired t-test analysis showed no statistically significant difference between the automatic determinations and any of the manual determinations of ϑ and ϕ ($p > 0.05$), as reported in Table 1 together with the mean, the s.d. and the range of the paired differences between measurements.

Figure 6 shows, for all ^{99m}Tc-sestamibi studies, the trans-

TABLE 1
Comparison of Automatic and Manual Techniques for Determining Transaxial Angles ϑ and Vertical Long-axis Angles ϕ Used in Reorienting 400 Myocardial Perfusion SPECT Images*

	Angle	Isotope	p†	Mean ± s.d. (°)	Range (°)	r	s.e.e. (°)
Auto vs. A	ϑ	^{201}Tl	ns	3.51 ± 3.00	0–16	0.902	4.19
	ϑ	^{99m}Tc-sestamibi	ns	3.53 ± 2.69	0–15	0.913	3.98
Auto vs. B1	ϑ	^{201}Tl	ns	2.56 ± 2.54	0–20	0.933	3.48
	ϑ	^{99m}Tc-sestamibi	ns	2.20 ± 1.81	0–10	0.957	2.82
Auto vs. B2	ϑ	^{201}Tl	ns	2.95 ± 2.22	0–13	0.930	3.56
	ϑ	^{99m}Tc-sestamibi	ns	2.43 ± 1.65	0–7	0.953	2.95
Auto vs. A	ϕ	^{201}Tl	ns	3.31 ± 2.90	0–18	0.851	4.41
	ϕ	^{99m}Tc-sestamibi	ns	2.40 ± 1.99	0–11	0.927	3.11
Auto vs. B1	ϕ	^{201}Tl	ns	2.54 ± 2.25	0–12	0.914	3.40
	ϕ	^{99m}Tc-sestamibi	ns	2.05 ± 1.82	0–10	0.959	2.34
Auto vs. B2	ϕ	^{201}Tl	ns	2.85 ± 2.22	0–12	0.904	3.59
	ϕ	^{99m}Tc-sestamibi	ns	2.20 ± 1.85	0–12	0.942	2.78

*The values for r and the s.e.e. derived from linear regression analysis refer to the graphs in Figure 5. Paired t-test analysis established that the angular values ϑ and ϕ obtained using the automated algorithm did not significantly differ from those estimated by human operators A, B1 and B2.
†p values are derived from results of paired t-test (significance level = 0.05).

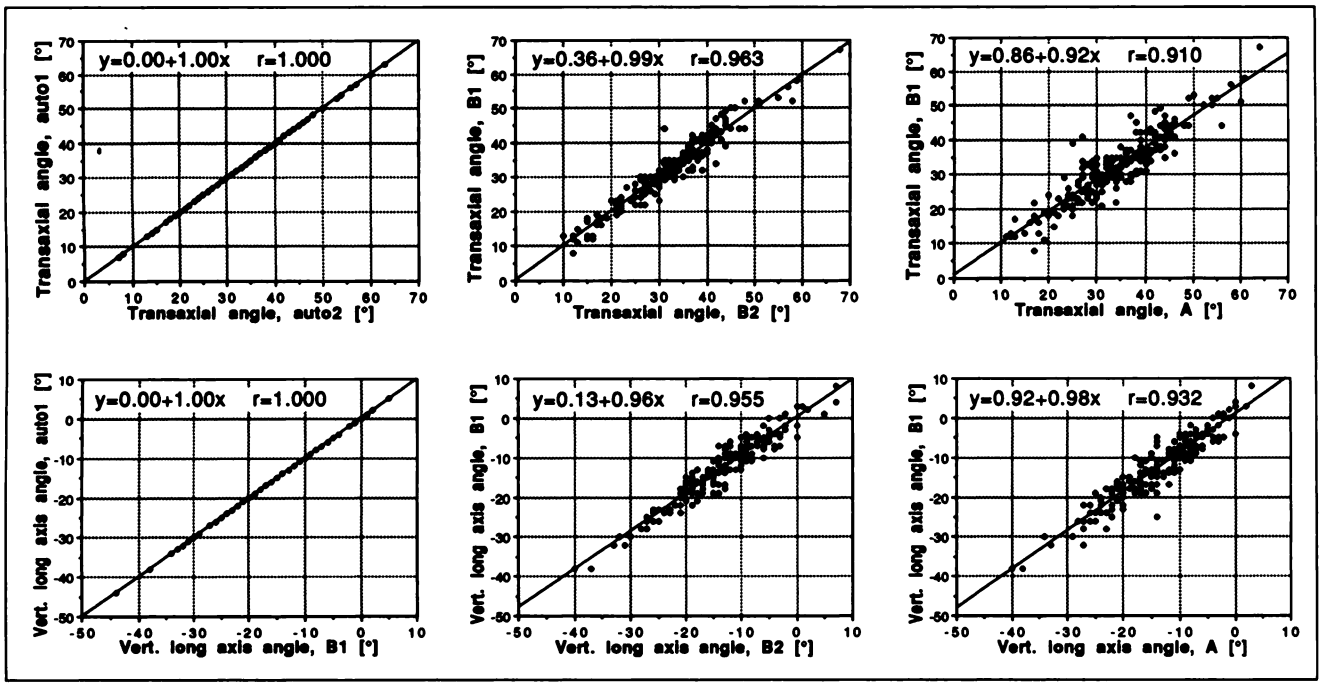

FIGURE 6. Automated algorithm reproducibility (left), intraobserver reproducibility (center) and interobserver reproducibility (right) for the transaxial angle ϑ (top row) and the vertical long axis angle ϕ (bottom row), for the 200 ^{99m}Tc-sestamibi studies analyzed. Note the perfect reproducibility of the automated technique for both ϑ and ϕ.

axial angle ϑ (top row) and the vertical long axis angle ϕ (bottom row) calculated by the automated software in two separate occasions (algorithm reproducibility, left), by operator B on two separate occasions (intraobserver reproducibility, center), and by operator A compared to operator B (interobserver reproducibility, right). Figure 6 and Table 2 show that reproducibility was perfect for the automatic technique (r = 1.000) and good to excellent for the manual technique. With regard to the latter, linear regression analysis resulted in r values, for manual B1 versus manual B2 and for manual B1 versus manual A, equal to 0.931 and 0.914 (ϑ, ^{201}Tl), 0.963 and 0.910 (ϑ, ^{99m}Tc-sestamibi), 0.937 and 0.906 (ϕ, ^{201}Tl) and 0.955 and 0.932 (ϕ, ^{99m}Tc-sestamibi), respectively. Table 2 also shows that the regressions' s.e.e. was 0° for the automatic algorithm, 2° to 4° for the human operators.

Further analysis aimed at comparing the reproducibilities of the automatic and manual techniques, and employed paired t-test analysis applied to the absolute angular differences (|Δ angle| in Table 3, expressed as mean ± s.d.) associated with various reproducibilities. Eight different comparisons were made: algorithm reproducibility versus intraobserver reproducibility (for both ^{201}Tl and ^{99m}Tc-sestamibi); algorithm reproducibility versus interobserver reproducibility (for both ^{201}Tl and ^{99m}Tc-sestamibi); intraob-

TABLE 2
Automated Algorithm, Intraobserver and Interobserver Reproducibility in the Determination of ϑ and ϕ*

	Angle	Isotope	r	s.e.e. (°)
Auto2 vs. auto1 [Auto^2]	ϑ	^{201}Tl	1.000	0.00
	ϑ	^{99m}Tc-sestamibi	1.000	0.00
B1 vs. B2 [B^2]	ϑ	^{201}Tl	0.931	3.61
	ϑ	^{99m}Tc-sestamibi	0.963	2.63
B1 vs. A [BA]	ϑ	^{201}Tl	0.914	3.99
	ϑ	^{99m}Tc-sestamibi	0.910	4.04
Auto2 vs. auto1 [Auto^2]	ϕ	^{201}Tl	1.000	0.00
	ϕ	^{99m}Tc-sestamibi	1.000	0.00
B1 vs. B2 [B^2]	ϕ	^{201}Tl	0.937	2.65
	ϕ	^{99m}Tc-sestamibi	0.955	2.29
B1 vs. A [BA]	ϕ	^{201}Tl	0.906	3.23
	ϕ	^{99m}Tc-sestamibi	0.932	2.82

*The values r and the s.e.e. derived from linear regression analysis refer to the graphs in Figure 6. Note the perfect reproducibility of the automatic technique. All notations in brackets are synthetic notations and are used in Table 3.

TABLE 3
Statistical Comparison of Automated (Auto^2), Intraobserver (B^2) and Intraobserver (BA) Reproducibility*

	|Δ angle| vs. |Δ angle| (ϑ)	p (ϑ)	|Δ angle| vs. |Δ angle| (ϕ)	p (ϕ)
(Auto^2, ^{99m}Tc) vs. (B^2, ^{99m}Tc)	0.0 ± 0.0 vs. 1.9 ± 1.5	<0.0001	0.0 ± 0.0 vs. 2.0 ± 1.7	<0.0001
(Auto^2, ^{201}Tl) vs.(B^2, ^{201}Tl)	0.0 ± 0.1 vs. 2.6 ± 2.9	<0.0001	0.0 ± 0.1 vs. 2.2 ± 1.7	<0.0001
(Auto^2, ^{99m}Tc) vs. (BA, ^{99m}Tc)	0.0 ± 0.0 vs. 2.4 ± 1.8	<0.0001	0.0 ± 0.0 vs. 3.5 ± 2.8	<0.0001
(Auto^2, ^{201}Tl) vs. (BA, ^{201}Tl)	0.0 ± 0.1 vs. 3.0 ± 2.9	<0.0001	0.0 ± 0.1 vs. 2.3 ± 2.2	<0.0001
(B^2, ^{99m}Tc) vs. (BA, ^{99m}Tc)	1.9 ± 1.5 vs. 2.4 ± 1.8	<0.0001	2.0 ± 1.7 vs. 3.5 ± 2.8	<0.0001
(B^2, ^{201}Tl) vs. (BA, ^{201}Tl)	2.6 ± 2.9 vs. 3.0 ± 2.9	ns	2.2 ± 1.7 vs. 2.3 ± 2.2	ns
(B^2, ^{201}Tl) vs. (B^2, ^{99m}Tc)	2.6 ± 2.9 vs. 1.9 ± 1.5	<0.002	2.2 ± 1.7 vs. 2.0 ± 1.7	ns
(BA, ^{201}Tl) vs. (BA, ^{99m}Tc)	3.0 ± 2.9 vs. 2.4 ± 1.8	<0.01	2.3 ± 2.2 vs. 3.5 ± 2.8	<0.001

*Paired t-test analysis established that the automated algorithm is significantly more reproducible than a single or two different human operators, for both angles and isotopes considered.

server reproducibility versus interobserver reproducibility (again, for both ^{201}Tl and ^{99m}Tc-sestamibi); intraobserver reproducibility for ^{201}Tl versus ^{99m}Tc-sestamibi; and interobserver reproducibility for ^{201}Tl versus ^{99m}Tc-sestamibi. The results of the analysis are shown in Table 3 and established that the automated algorithm's reproducibility is significantly better than the intraobserver reproducibility or the interobserver reproducibility for both angles and isotopes considered ($p < 0.0001$). Intraobserver reproducibility is significantly better than interobserver reproducibility in ^{99m}Tc-sestamibi images for both angles considered ($p < 0.0001$), but there is no significant difference for ^{201}Tl images. Interobserver reproducibility is significantly better in ^{99m}Tc-sestamibi compared to ^{201}Tl images ($p < 0.01$ for the transaxial angle ϑ, $p < 0.001$ for the vertical long-axis angle ϕ), while intraobserver reproducibility is significantly better in ^{99m}Tc-sestamibi images for ϑ ($p < 0.002$), but not for ϕ.

DISCUSSION

The main problem in trying to validate any automatic reorientation technique is that the manual measurements used as a gold standard suffer from relatively high intra- and interobserver variability. If a human operator processing the same data sets twice generates two sets of angular values that agree at a given level r, one would not expect a better agreement when comparing one of those sets to values generated by an automated algorithm. In other words, the s.e.e. associated with the linear regression analysis of manual reproducibility defines the precision of our gold standard, which from Table 2 appears to range between 2° and 4°.

An interesting finding of this study was that intraobserver reproducibility was substantially equivalent to interobserver reproducibility in ^{201}Tl images (Table 3, row 6), despite the fact that the operator generating the data used for intraobserver analysis had previous knowledge of the algorithm on which the automatic method is based, and had in fact participated in its development. On the other hand, intraobserver reproducibility proved significantly superior to interobserver reproducibility for both transaxial and vertical long-axis angle determination in ^{99m}Tc-sestamibi images, generally considered of higher quality than ^{201}Tl images due to their better counting statistics and higher photon energy. Interobserver reproducibility (both angles) and intraobserver reproducibility (transaxial angle) were also significantly better in ^{99m}Tc-sestamibi compared to ^{201}Tl images, further supporting the hypothesis that high image quality may help make the task of manual reorientation easier.

The relatively low reproducibility of manual reorientation techniques is, at least in part, a consequence of the reorientation process itself being a poorly defined problem. Generating "short-axis images" perpendicular to the LV's long axis is possible if such an axis is uniquely determinable. This is true for an ellipsoid (or, more generally, for a quadratic surface), but the human heart often considerably departs from the ellipsoidal model, and, in some cases, is quite asymmetrical (Fig. 7). The LV's imperfect conformance to a simple geometric model poses problems for both manual and automatic reorientation techniques, but the former are at an additional disadvantage when fitting the LV to a particular geometry. The automatic algorithm performs fits in the three-dimensional space, while the human operator bases his judgment on 2 two-dimensional images: one in a transaxial and the other in a sagittal plane (Fig. 1). If the operator emulated the algorithm's ellipsoidal fit, he/she would have to visually fit ellipses to the myocardium as it appears in those two planes and gauge the ellipses' major axis, a nontrivial task at best. In search of simpler reori-

FIGURE 7. Midventricular transaxial images of four patients whose LV myocardium either does not conform to an ellipsoidal model (A–C) or is not completely visible due to perfusion defects (D). The absolute differences between the automatic and the manual (operator A) determinations of ϑ were 9°, 6°, 2° and 11° for cases A–D, respectively.

entation criteria, most operators draw the LV's long axis as a line passing through the LV's apex and parallel to, or equidistant from, the LV myocardial walls. Unfortunately, in many cases those two criteria are mutually exclusive, and in other cases true perfusion defects (especially apical) or attenuation artifacts obscure parts of the myocardium, making guesswork necessary (Fig. 7). With all these considerations in mind, it is indeed not difficult to understand how a human operator's accuracy in determining the orientation of the LV's long axis would be, on average, not better than a few degrees.

As a final test, for each of the 400 reoriented images, the angles ϑ and ϕ determined by the automated algorithm were overlayed onto a transaxial and a sagittal plane and presented to a human operator (B) for evaluation. The operator judged all but 9 of the 400 studies to have been reoriented in an acceptable manner by the algorithm, further stressing the fact that, within a few degrees' range, several angular values may appear "reasonable" in manual reorientation. The effect of variability in the manual estimates of ϑ and ϕ on the visual and quantitative evaluation of the final reoriented images should be investigated in a large series of patients to determine the minimal level of intra- and interobserver reproducibility necessary to ensure accurate and consistent image interpretation.

CONCLUSION

We have developed a method for the automatic reorientation of myocardial perfusion SPECT images. The technique operates with 98.5% success, is perfectly reproducible and agrees very well with the results of manual reorientation. The automatic reorientation algorithm consists of three steps: segmentation of the LV myocardium, extraction of the LV's mid-myocardial surface and fit of that surface to an ellipsoid, whose major axis identifies the long axis of the LV. In its current implementation on a relatively inexpensive (<$5,000), off-the-shelf computer, the algorithm is fast, portable and does not require any proprietary hardware or special pre-reorientation processing. Considering the difficulty and imperfect reproducibility of manual reorientation of three-dimensional images, it is conceivable that automatic reorientation could become the gold standard for this task.

Automatic reorientation can be performed on a series of clinical myocardial SPECT studies in batch mode, without the need for operator intervention or supervision. The algorithm is able to use a combination of knowledge-based rules (i.e., location of the LV cluster, goodness of the ellipsoidal fit and orientation of the ellipsoid axes) to estimate the likelihood of its having correctly reoriented the image data set. Studies with a high likelihood of error can be marked for later re-examination by a human operator. Automatic reorientation is an important step towards the totally automated processing of myocardial SPECT data. The integration of reorientation with other software modules performing automatic reconstruction of the transaxial images from the projection data, automatic quantification of the short-axis images (*4,16–18*) and automatic diagnostic interpretation of the quantitative results through expert systems (*19,20*) and neural networks (*21*) is being investigated at our institution, as well as at other centers with the final goal of implementing a complete, objective and reproducible approach to the processing and analysis of myocardial SPECT and PET images.

REFERENCES

1. Hoffman EJ, Huang SC, Phelps ME. Quantitation in positron emission tomography: I. Effect of object size. *J Comput Assist Tomogr* 1979;3:299–308.
2. Senda M, Yonekura Y, Tamaki N, et al. Interpolating scan and oblique-angle tomograms in myocardial PET using nitrogen-13 ammonia. *J Nucl Med* 1986;27:1830–1836.
3. Kuhle WG, Porenta G, Huang SC, Phelps ME, Schelbert HR. Issues in the quantitation of reoriented cardiac PET images. *J Nucl Med* 1992;33:1235–1242.
4. Garcia E, Van Train K, Maddahi J, et al. Quantification of rotational thallium-201 myocardial tomography. *J Nucl Med* 1985;26:17–26.
5. Borrello JA, Clinthorne NH, Rogers WL, Thrall JH, Keyes JW. Oblique-angle tomography: a reconstructing algorithm from transaxial tomographic data. *J Nucl Med* 1981;22:471–473.
6. Lancaster JL, Starling MR, Kopp DT, Lasher JC, Blumhardt R. Effect of errors in reangulation on planar and tomographic thallium-201 washout profile curves. *J Nucl Med* 1985;26:1445–1455.
7. DePuey EG, Garcia EV. Optimal specificity of thallium-201 SPECT through recognition of imaging artifacts. *J Nucl Med* 1989;30:441–449.
8. Cooke CD, Folks RD, Jones ME, Ezquerra NF, Garcia EV. Automatic program for determining the long axis of the left ventricular myocardium used for thallium-201 tomographic reconstruction [Abstract]. *J Nucl Med* 1989;30:806.
9. He ZX, Maublant JC, Cauvin JC, Veyre A. Reorientation of the left ventricular long axis on myocardial transaxial tomography by a linear fitting method. *J Nucl Med* 1991;32:1794–1800.
10. Cauvin JC, Boire JY, Maublant JC, Bonny JM, Zanca M, Veyre A. Automatic detection of the left ventricular myocardium long axis and center in thallium-201 single-photon emission computed tomography. *Eur J Nucl Med* 1992;19:1032–1037.
11. Serra J. *Image analysis and mathematical morphology.* London: Academic Press; 1984.
12. Berman DS, Kiat H, Friedman JD, et al. Separate acquisition rest thallium-201/stress technetium-99m-sestamibi dual isotope myocardial perfusion SPECT: a clinical validation study. *J Am Coll Cardiol* 1993;22:1455–1464.
13. Kiat H, Germano G, Friedman J, et al. Comparative feasibility of separate or simultaneous rest thallium-201/stress technetium-99m sestamibi dual isotope myocardial perfusion SPECT. *J Nucl Med* 1994;35:542–548.
14. Germano G, Van Train K, Garcia E, et al. Quantitation of myocardial perfusion with SPECT: current issues and future trends. *Nuclear cardiology: the state of the art and future directions.* St Louis: Mosby Year Book; 1992:77–88.
15. Winston PH. *Artificial intelligence,* third edition. Reading, MA: Addison-Wesley; 1992:66–68.
16. Van Train K, Berman DS, Garcia E, et al. Quantitative analysis of stress ^{201}Tl myocardial scintigrams: a multicenter trial. *J Nucl Med* 1986;31:1168–1180.
17. Garcia EV, Cooke CD, Van Train KF, et al. Technical aspects of myocardial SPECT imaging with technetium-99m-sestamibi. *Am J Cardiol* 1990;66:23E–31E.
18. Van Train KF, Areeda J, Garcia EV, et al. Quantitative same-day rest-stress technetium-99m-sestamibi SPECT: definition and validation of stress normal limits and criteria for abnormality. *J Nucl Med* 1993;34:1494–1502.
19. Horino M, Hosoba M, Wani H, et al. Development and clinical application of an expert system for supporting diagnosis of Tl-201 stress myocardial SPECT. *Jpn J Nucl Med* 1990;27:93–106.
20. Garcia E, Cooke D. Computer methods in nuclear cardiology. In: *Nuclear cardiology: the state of the art and future directions.* St Louis: Mosby Year Book; 1992:97–108.
21. Fujita H, Katafuchi T, Uehara T, Nishimura T. Application of artificial neural network to computer-aided diagnosis of coronary artery disease in myocardial SPECT bull's-eye images. *J Nucl Med* 1992;33:272–276.